Journal of Nuclear Materials xxx (xxxx) xxx

Contents lists available at ScienceDirect

Journal of Nuclear Materials

journal homepage: www.elsevier.com/locate/jnucmat

In search of θ-(Pu,Zr) in binary Pu–Zr: Thermal and microstructural analyses of Pu – 30Zr alloy

Assel Aitkaliyeva [a, *], Cynthia A. Adkins [a, b], Casey McKinney [a], Jacob Hirschhorn [a], Michael R. Tonks [a]

[a] Department of Materials Science & Engineering, University of Florida, Gainesville, FL, 32611, USA
[b] Idaho National Laboratory, Idaho Falls, ID, 83415, USA

ARTICLE INFO

Article history:
Received 16 July 2019
Received in revised form
22 September 2019
Accepted 28 October 2019
Available online xxx

Keywords:
Plutonium-zirconium
Metallic fuel
Microstructure
Phase identification
Phase transition temperatures

ABSTRACT

The existing Pu–Zr binary phase diagrams report the stability of the compound θ-(Pu,Zr) in the low temperature region between 300 and 0 °C. Furthermore, the current understanding is that θ-(Pu–Zr) is thermodynamically favored over the metastable δ-(Pu,Zr) phase. In an effort to shed light on the phases formed in Pu–Zr binary alloys and reduce uncertainties in the poorly defined boundary between the θ-(Pu,Zr), (θ+δ), δ-(Pu,Zr), and (θ+α-Zr) regions, Pu – 30Zr (in wt.%, equivalent 53 at.%) alloys were subjected to microstructural characterization, annealing, and differential scanning calorimetry (DSC). The results indicate that the alloy is composed of δ-(Pu,Zr) matrix, with a number of smaller, randomly distributed α-Zr precipitates. The phase transition temperatures (determined based on the DSC data) and phases identified in Pu – 30Zr alloys (based on crystallographic data) compare well to those predicted by the phase diagrams with the exception of the θ-(Pu–Zr) phase. Our data indicates that θ-(Pu–Zr) is metastable and can be observed only within a small temperature window (100–300 °C). The consecutive heating cycles remove θ-(Pu–Zr) from the system, and no traces of θ-(Pu–Zr) remain at room temperature, as evidenced by microstructural characterization. This calls for reevaluation of the binary Pu–Zr phase diagram, with particular attention paid to the existence of θ-(Pu–Zr) and its stability.

1. Introduction

The complex and time-varying microstructure of metallic fuels contributes to and evolves with a number of coupled irradiation behaviors, which negatively influence the performance of metallic fuel elements. Because of this complexity, the metallic U-Pu-Zr fuels are lacking a sound scientific foundation for the development of computational models that can mechanistically predict their behavior. In this contribution, we scrutinize the phases in binary Pu–Zr alloys as a first step to understanding the thermodynamic behavior of ternary U-Pu-Zr fuels.

The key features of the Pu–Zr phase diagram (provided in Fig. 1 for the reader's convenience) are continuous solubility between β-Zr and ε-Pu, extensive solubility of Zr in δ-Pu, limited solubility of Zr in α-Pu, β-Pu, γ-Pu, and δ′-Pu, and existence of the θ-(Pu–Zr) intermediate phase, which is stable at room temperature [1]. The Pu-rich (80–100 at.% Pu) portion of the phase diagram is debated by a number of research groups [1–9]. Our previous work has indicated that heat treatment will anneal out metastable κ-$PuZr_2$ from Pu – 10Zr (in wt.%, equivalent to 12 at.%) and result in formation of δ′-Pu and β-Pu phases within δ-(Pu,Zr) matrix [7].

To avoid the complexities of Pu-rich region, this manuscript focuses on the less frequently debated part of the phase diagram (50–60 at.% Zr/50–40 at.% Pu), denoted with the red box in Fig. 1. The alloy exists in liquid form at high temperatures (>1350 °C) and transitions to a mixture of liquid and (ε-Pu,β-Zr) solid solution upon cooling. Further cooling leads to decomposition of (ε-Pu,β-Zr) into the mixture of (ε-Pu,β-Zr) and δ-(Pu,Zr), followed by transition into δ′-Pu and then δ-(Pu,Zr) around 580 °C. Around 250 °C, phase diagrams indicate that δ-(Pu,Zr) will start transforming into intermetallic θ-(Pu–Zr), and then mixture of θ-(Pu–Zr) and α-Zr, which is predicted to be stable between 300 °C and room temperature (RT).

Of particular interest to this contribution was the region between 550 °C and RT, which should include primarily δ-(Pu,Zr) and θ-(Pu–Zr) matrix with α-Zr precipitates. These precipitates are

* Corresponding author. 176 Rhines Hall, Department of Materials Science and Engineering, University of Florida, PO Box 116400, Gainesville, FL, 32611-6400, USA
E-mail address: aitkaliyeva@mse.ufl.edu (A. Aitkaliyeva).

https://doi.org/10.1016/j.jnucmat.2019.151875
0022-3115/

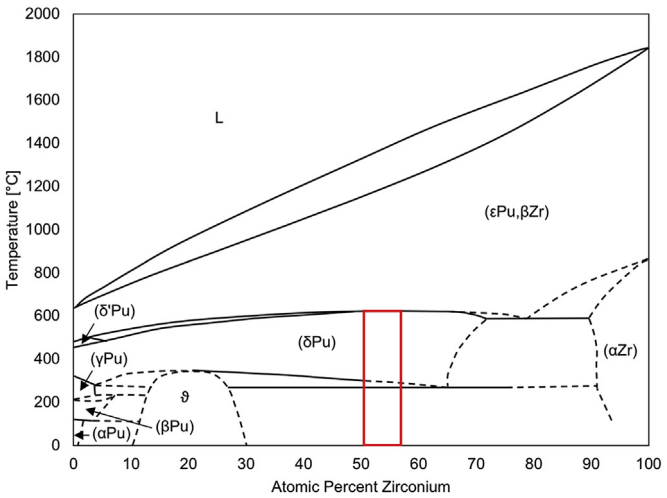

Fig. 1. Reproduction of the Pu–Zr phase diagram as given in Ref. [1], where the alloy under consideration are marked in red and the more frequently contested κ-$PuZr_2$, ι-(Pu,Zr), and ζ-$Pu_{28}Zr$ phases are not shown. Dashed lines, such as the one that defines the θ-(Pu–Zr) stability region, indicate portions of the phase diagram with particularly high uncertainty. (For interpretation of the references to colour in this figure legend, the reader is referred to the Web version of this article.)

commonly referred to as "oxygen-stabilized α-Zr," but little is known about their formation mechanisms [10–12]. The compound θ-(Pu,Zr) (also known as Pu_4Zr or Pu_6Zr) has been said to occur at about 20 at.% Zr but has been notoriously difficult to observe experimentally [3]. If the phase diagram shown in Fig. 1 is accurate, it can be assumed that even if the matrix phase does not predominantly consist of θ-(Pu,Zr), it should contain at least traces of θ-(Pu,Zr). However, little to no agreement over the (θ+α-Zr) region exists, and further work is needed to determine the transition points for these phases.

The goal of this manuscript is to compare the experimental data to the existing phase diagrams and determine if the current understanding of the Pu–Zr system is sufficient for development of accurate computational models of its microstructure. To this end, we conducted microstructural characterization of Pu – 30Zr alloys and investigated the phases formed in this binary system using microscopy-based techniques. The phase transition temperatures were determined and correlated to the observed microstructural features, and gaps in the community's scientific understanding of these alloys were identified.

2. Materials and methods

Alloys with nominal compositions of Pu – 30Zr (in wt.%, equivalent 53 at.%) were fabricated in a similar fashion to the metallic (U-Pu-Zr) fuel alloys. The alloys were arc cast in an inert atmosphere glovebox containing <50 parts per million (ppm) oxygen and homogenized between consecutive melts. The cast slugs were sectioned into pieces for microscopy and thermodynamic property measurements. The described arc casting procedure has been routinely used to produce metallic U and Pu fuel alloys for the past 20 years and our previous experience indicates that the nominal compositions of the cast alloys match the desired compositions. The compositions of the cast specimens, including those selected for this study, have been verified with inductively coupled plasma mass spectroscopy technique prior to characterization work.

After casting, the surfaces of all fuel pieces were polished through 1200 grit SiC paper to remove surface damage from cutting and possible oxidation layers. Some of the specimens were annealed at 550 °C for 17 h in a furnace and allowed to cool to ambient temperatures (at a rate of ~20 °C/min) under continuous argon flow containing 0.6–1.2 ppm oxygen. The rationale for selecting an annealing temperature of 550 °C is based on the following. The selected temperature is sufficiently high to bring the system close to the equilibrium while avoiding the complexity associated with (ε-Pu, β-Zr) and liquid phases favorable at higher temperatures. Since all phase diagrams consistently predict formation of the θ-(Pu–Zr) below 300 °C, the selected annealing temperatures were deemed to be acceptable for preliminary studies.

All specimens for microstructural characterization were embedded in epoxy and polished down to 0.25 μm to remove surface damage layers. The polished specimens were coated with a ~30 nm thick gold layer to prevent charging during imaging. Both as-cast and annealed specimens were examined first in a JEOL JSM 700 field emission scanning electron microscope (SEM), followed by specimen milling in an FEI Quanta 3D field emission gun (FIG) focused ion beam (FIB) instrument, and analysis in an FEI Tecnai TF-30-FEG scanning/transmission electron microscope (S/TEM). The accelerating voltages of the instruments varied: the SEM was operated at 20 kV, the TEM at 300 kV, and the FIB at 30 kV (milling steps at ±1.5°), 5 kV (initial cleaning step at ±5°), and 2 kV (final cleaning step at ±5°).

Specimens for TEM were prepared in a dual beam FIB/SEM instrument using a standard lift-out procedure [7]. Up to ten cross-sectional lamellae (each approximately 20 μm × 10 μm × 0.09 μm in size) were prepared to ensure that all phases were captured. Note that the specimens were examined for beam damage following specimen preparation to ensure that Ga-induced artifacts would not interfere with phase identification. The microstructure of the lamellae were examined in the S/TEM and phase identification was conducted by comparing experimentally collected selective area electron diffraction (SAED) patterns and measured lattice spacing to those from published crystal structures [2–4,8,9,12,13]. Pearson's Crystal Data crystallographic database [14] was used to create input files for CrystalMaker software [15], which aided in visualization of the crystal structure of individual phases.

Authors recognize that TEM-based SAED analysis is localized and might not capture all phases present in the bulk alloy. When conducting phase identification, it is advisable to use bulk techniques such as X-ray diffraction (XRD), SEM and electron backscatter diffraction (EBSD) that can capture all the phases present on the surface of the fuel alloys. Note that the surface of the bulk specimens was thoroughly examined in SEM secondary and backscattered electron imaging and energy and wavelength dispersive spectroscopy (EDS/WDS) techniques prior to FIB lift-out procedure. The resulting quantitative chemical analysis data for Pu-based phases are questionable in nature due to the lack of commercially available (or home-made) Pu standards and qualitative data is not sufficient for precise phase identification. The location of the lift-outs for TEM analysis were selected randomly to avoid operator bias and capture all phases forming in the alloy.

The phase transition temperature and enthalpies for phase formation were established by analyzing the alloys in a NETZCH Differential Scanning Calorimeter (DSC) model DSC404 F1 Pegasus using MgO lined Pt/Rh crucibles. The instrument was located inside of an inert atmosphere glovebox, in which the oxygen levels were controlled in the sub-parts per billion range. The data collection was performed between ambient temperature and 700 °C at a constant rate of 10 °C/min. The cooling and heating rate of 10 °C/min was selected for the DSC runs because it provided the best compromise between resolving overlapping peaks for phase transition analysis and reproducing reactor conditions for specific heat

Please cite this article as: A. Aitkaliyeva et al., In search of θ-(Pu,Zr) in binary Pu–Zr: Thermal and microstructural analyses of Pu – 30Zr alloy, Journal of Nuclear Materials, https://doi.org/10.1016/j.jnucmat.2019.151875

capacity data. Three consecutive thermal cycles were performed to ensure consistency of the results. To match the annealing conditions performed on specimens for microscopy, the DSC specimen was annealed at 555 °C for 16.93 h between the second and third thermal cycles.

The DSC instrument was calibrated prior to alloy analysis for both temperature and heat flow sensitivity using ASTM E967-18 "Standard Test Method for Temperature Calibration of DSC and DTA" and ASTM E968-02 (2014) "Standard Practice for Heat Flow Calibration of DSC". The temperature calibration was conducted using a set of melting point standards provided by the instrument vendor (In, Zn, Al, Ag, Au, and Ni), where each material was heated through its melting temperature, that temperature was plotted verses literature values, and a correction curve was generated for the sample thermocouple. The heat flow sensitivity was calibrated using a single crystal sapphire reference material and it was heated through the same temperature and rate profile as the specimen runs. These data on the sapphire are compared to literature and a correction curve was generated. Both correction curves are activated during all specimen measurements including baselines.

3. Results and discussion

Both as-cast and annealed alloys were examined in an SEM, and the backscattered electron micrographs from both specimens are shown in Fig. 2. The microstructure of the as-cast alloy contained a large number of darker Zr-rich inclusions, which were uniformly distributed across the lighter contrast Pu–Zr matrix (Fig. 2(a)). Annealing refined the microstructure of the alloy and brought the system closer to the equilibrium, as can be seen from Fig. 2(b), in which Zr-rich inclusions increase in size but decrease in number. The overall microstructure of the as-cast and annealed specimens looked similar in the SEM, and thus further characterization was conducted in TEM, which has higher resolution and allows microstructural features to be discerned in more detail.

The lamellae for TEM analysis were lifted-out from random locations across the specimen surfaces, some of which can be seen on the bottom left corner of Fig. 2(a). Up to ten cross-sectional lamellae were prepared from each as-cast and annealed alloys, and at least five SAED patterns at varying zone axes were collected from individual phases observed in all lamella to increase statistical significance. Note that while four lamellae were lifted-out from one area, other lamellae were spaced far apart to make sure all phases have been captured. The X-ray spectra were collected from corresponding phases and used to guide the phase identification process. Nonetheless, the phase identification primarily relied on measurement of the lattice spacing of a particular diffraction pattern, which was compared to the crystallographic data published in the literature [2–4,8,9,12,13]. Note that experimental SAED patterns were evaluated against all possible phases predicted for Pu–Zr alloys to identify the best match. Since hundreds of SAED patterns were acquired and the obtained results were consistent throughout all examined specimens, we will provide the representative results in this manuscript.

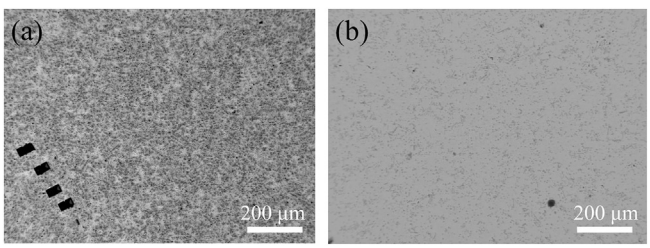

Fig. 2. Backscattered electron micrographs of the Pu – 30Zr alloy: (a) before and (b) after annealing at 550 °C. The scale bar denotes 200 μm in both micrographs. The black rectangles on the left side of (a) denote the lift-out areas of four of the ten TEM lift-outs.

Fig. 3 shows the STEM micrographs at varying magnifications acquired from as-cast Pu – 30Zr alloy (top row), experimentally obtained SAED patterns of the individual phases (middle row, in white), and simulated SAED patterns (bottom row, in blue) corresponding to the experimental data. Note that STEM micrographs include both lower (on the left) and higher magnification (on the right) views of the as-cast microstructure. As can be seen from Fig. 3, the light contrast matrix was consistent with face-centered cubic (fcc) δ-(Pu,Zr) phase, and the inclusions were consistent with hexagonal close packed (hcp) α-Zr. A monoclinic ZrO_2 precipitate was found in only one of the examined lamellae close to the specimen surface, which was likely stabilized by the impurities during casting of the alloys.

Fig. 4 shows the STEM micrographs at varying magnifications, experimentally obtained SAED patterns (in white), and simulated SAED patterns (in blue) of the individual phases observed in the annealed Pu – 30Zr alloy. Overall, the microstructure of the annealed specimen was similar to the as-cast alloy and agreed well with SEM observations. The matrix was consistent with fcc δ-(Pu,Zr) and the inclusions were consistent with hcp α-Zr. However, annealing resulted in coarsening of the precipitates: a large number of smaller α-Zr inclusions seen in as-cast alloy transformed into fewer but larger α-Zr islands in the annealed specimen.

Based on the microstructural characterization results (Figs. 3 and 4), no traces of θ-(Pu,Zr) were found in either of the alloys – as-cast or annealed. Readers are reminded that the phase diagram (Fig. 1) predicts that within selected composition and temperature range, alloys should have matrix consisting of δ-(Pu,Zr) at elevated temperatures and θ-(Pu–Zr) with α-Zr at room temperature. Our observations show a large number of oddly shaped α-Zr precipitates throughout the alloys, which suggests that the as-cast specimens were not at equilibrium. The casting process is not completely impurity free (the glovebox is kept at <50 ppm oxygen), and even traces of impurities (in the tens of ppm range) can stabilize the α-Zr phase. Note that the exact impurity responsible for stabilization of α-Zr has yet to be confirmed. This would require analytical chemistry analyses, but the techniques currently available are not equipped to analyze Pu-based fuel alloys for oxygen and carbon content. The stability of the α-Zr at high temperatures exceeds that of the δ-(Pu,Zr) matrix (>800 °C vs ~600 °C) and the annealing temperature selected in this work (550 °C), which explains why α-Zr was retained upon annealing.

In addition to the primary microstructural differences between the as-cast and annealed alloys, finer microstructural features were noted in the examined specimens. While annealing did not alter the primary phases present in the alloys, it is clear that several distinctive microstructural changes occurred upon annealing. The top row of Fig. 5 provides lower and higher magnification overviews of the matrix δ-(Pu,Zr) and α-Zr inclusions seen in as-cast Pu – 30Zr alloy. Note the fine grain sizes (1.8 μm) of the matrix phase in as-cast specimen (see Fig. 5(a)), where a few grains have been highlighted with white triangles. The grain sizes were measured using ImageJ software.

The α-Zr precipitates have a defined shape and do not seem to contain any other inclusions, unlike those in the annealed alloy. Annealing leads to apparent segregation of an additional phase in α-Zr inclusions, as evidenced by the light objects within the α-Zr precipitates in Fig. 5(c)–(d). The fine nature of the precipitation did not allow for phase identification: collected SAED patterns matched those of the background α-Zr. Similarly, TEM-based X-ray analysis of these inclusions indicated that the composition did not change

Please cite this article as: A. Aitkaliyeva et al., In search of θ-(Pu,Zr) in binary Pu–Zr: Thermal and microstructural analyses of Pu – 30Zr alloy, Journal of Nuclear Materials, https://doi.org/10.1016/j.jnucmat.2019.151875

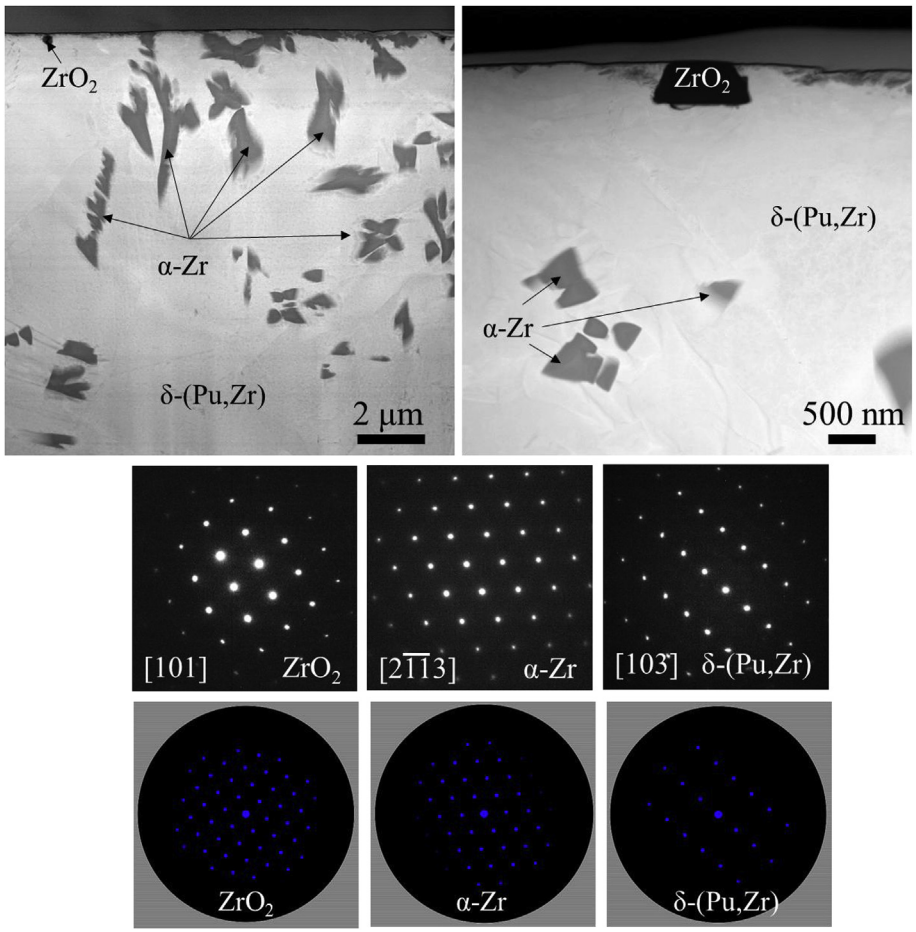

Fig. 3. Phases observed in the as-cast Pu – 30Zr alloy: top row are the STEM micrographs of the phases (acquired at two magnifications: lower (on the left) and higher (on the right), scale bars denote 2 μm and 500 nm) and bottom rows experimental (in white) and simulated (in blue) SAED patterns corresponding to each phase. (For interpretation of the references to colour in this figure legend, the reader is referred to the Web version of this article.)

upon annealing and that the additional phase had the same composition as α-Zr. However, further work will be conducted in the future to determine what causes the segregation within α-Zr and whether a secondary phase indeed forms within α-Zr.

Annealing resulted in coarsening of the grains, with average grain size increasing to 2.5 μm. Furthermore, preferential grain boundary oxidation has occurred in the annealed alloys, which are denoted by red arrows in Fig. 5(c)–(d). As Pu is known for its affinity to oxygen, oxidation of the alloy is to be expected considering that oxygen impurities (in ppm range) can remain in the glovebox during annealing. It is well known that grain boundaries serve as preferential defect and impurity sinks in solids since the distance between adjacent grain faces is greater than atomic spacing inside the grain. It is thus not surprising to see preferential oxidation of matrix δ-(Pu,Zr) phase along grain boundaries. Note that similar grain boundary oxidation has been noted in previously examined annealed Pu – 10Zr alloy [7].

The primary difference between our data and predicted phase diagrams is the absence of the θ-(Pu,Zr) phase. Our detailed characterization at various length scales would have detected this phase if it indeed formed in Pu–Zr alloys. We conducted further analyses in a DSC to determine the nature of this discrepancy. Fig. 6 shows the DSC profiles for the Pu – 30Zr alloy, where phase transformations through three heating and cooling cycles are given as individual plots in (a-c). Note that Fig. 6(a)–(b) correspond to the as-cast alloy, which was annealed at 555 °C after completion of the second DSC cycle. The data on the annealed alloy is provided in Fig. 6(c). The alloys undergo endothermic phase transition during heating and exothermic phase transition during cooling cycles. These DSC measurements were used to determine the phase transition temperatures, which are provided in Tables 1 and 2

During the initial heating of the as-cast alloy (Fig. 6(a)), a broad valley resembling a peak was observed between 268 °C and 320 °C (see black arrow on the plot). Another feature of interest in the initial heating curve is a broad peak ranging from 630 °C to 660 °C. The only notable feature of interest in the cooling curve is the peak ranging from 600 °C to 620 °C, which is retained through all thermal cycles and annealing. The heating curve, on the other hand, changes slightly after initial thermal cycle. The broad valley observed between 268 °C and 320 °C disappears from the heating curve of the as-cast alloys upon consecutive thermal cycles (illustrated by the black arrow in Fig. 6(b)). The DSC curves of the annealed alloy are similar to that of the as-cast alloy after the second thermal cycle and are provided in Fig. 6(c).

To aid with visualization of the phase transformations occurring in the system, Fig. 6(a) imposes phase transition lines (denoted with dashed vertical lines) predicted by the phase diagram (Fig. 1) onto the DSC data of the as-cast alloy. This DSC data set was selected for this discussion since it has several distinct features as compared to all other runs. Overall, the onset and end temperatures at which peaks occur during heating agree well with the predicted Pu–Zr phase diagram, as can be seen from Fig. 6(a). Below 300 °C,

Please cite this article as: A. Aitkaliyeva et al., In search of θ-(Pu,Zr) in binary Pu–Zr: Thermal and microstructural analyses of Pu – 30Zr alloy, Journal of Nuclear Materials, https://doi.org/10.1016/j.jnucmat.2019.151875

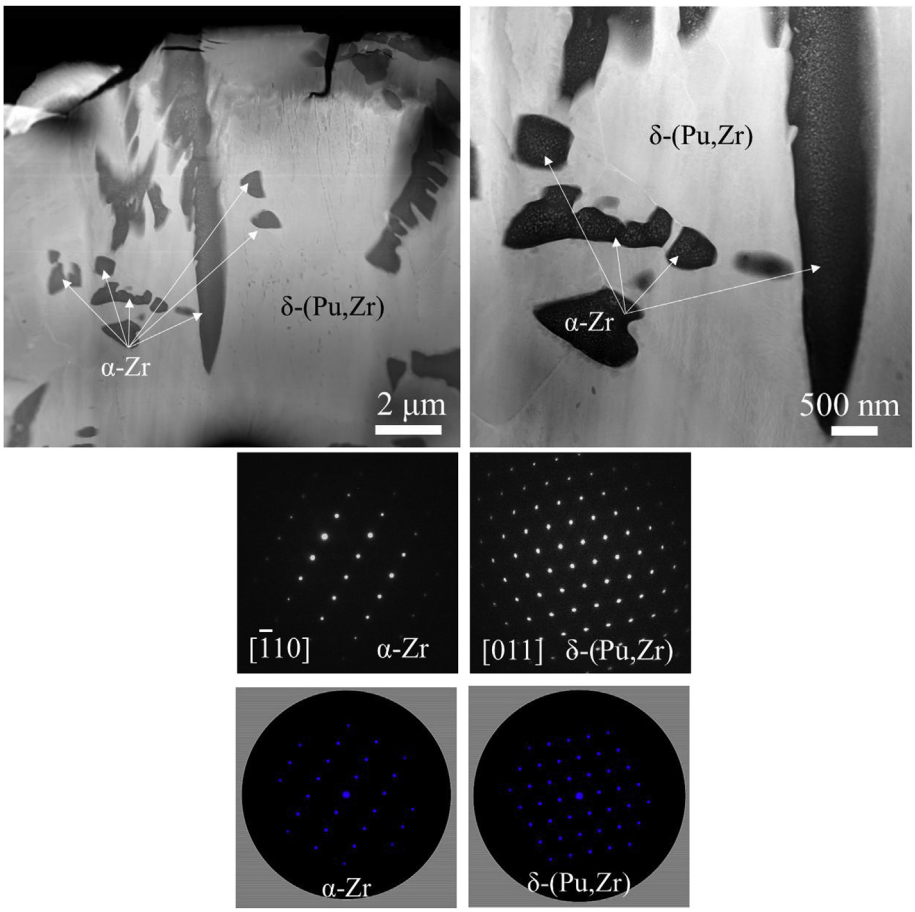

Fig. 4. Phases observed in the annealed Pu – 30Zr alloy: top row are the STEM micrographs of the phases (acquired at two magnifications: lower (on the left) and higher (on the right), scale bars denote 2 μm and 500 nm) and bottom rows experimental (in white) and simulated (in blue) SAED patterns corresponding to each phase. (For interpretation of the references to colour in this figure legend, the reader is referred to the Web version of this article.)

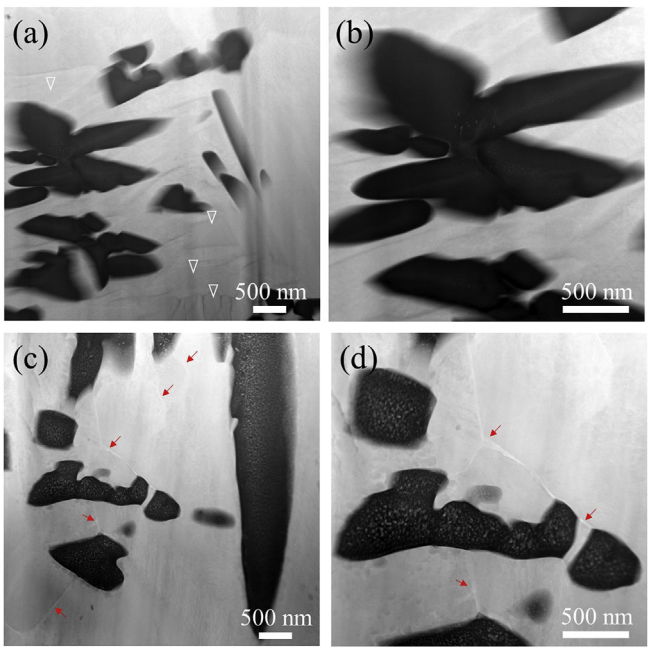

Fig. 5. STEM micrographs of the as-cast (a)–(b) and annealed (c)–(d) Pu – 30Zr alloys. White triangles and red arrows identify grains and grain boundaries, respectively. The scale bars denote 500 nm. (For interpretation of the references to colour in this figure legend, the reader is referred to the Web version of this article.)

one can assume the presence of θ-(Pu–Zr) and α-Zr, or δ-(Pu,Zr) and α-Zr, which yields to stabilization of δ-(Pu,Zr) upon further heating. The existence of θ-(Pu–Zr) and δ-(Pu,Zr) two phase region is predicted by the phase diagrams but this region is small and likely could not be discerned by DSC. Between 300 °C and 600 °C, the matrix retains its δ-(Pu,Zr) structure, which eventually transforms into (ε-Pu,β-Zr) solid solution, with predicted onset temperature of ~630 °C. Note that presence of the δ′-Pu is possible but limited sensitivity of the technique, combined with rapid heating/cooling rates, would not allow resolution of the phase within DSC peaks. Consequent cooling of the alloy leads to decomposition of the (ε-Pu, β-Zr) into the mixture of (ε-Pu, β-Zr) and δ-(Pu,Zr), of which only δ-(Pu,Zr) is retained at lower temperatures. Further cooling does not initiate the decomposition of δ-(Pu,Zr) into other phases. The broad valley observed between 268 °C and 320 °C in the heating curve of the as-cast alloys can be attributed to formation of a temporary phase. However, this temporary phase was eliminated by the consecutive heating cycle and is not present in the annealed alloy, which indicates its metastable nature. Based on the obtained data, the phase transition temperatures and phases identified in Pu – 30Zr alloys compare well to those predicted by the phase diagrams with the exception of the θ-(Pu–Zr) phase.

We therefore postulate that the existing phase diagrams are incorrect in predicting the regions in which θ-(Pu–Zr) is stable in the binary Pu–Zr system. This is not surprising considering that the phase transition lines for θ-(Pu–Zr) have not been confirmed to this date. Plutonium phase transformations are known for their

Please cite this article as: A. Aitkaliyeva et al., In search of θ-(Pu,Zr) in binary Pu–Zr: Thermal and microstructural analyses of Pu – 30Zr alloy, Journal of Nuclear Materials, https://doi.org/10.1016/j.jnucmat.2019.151875

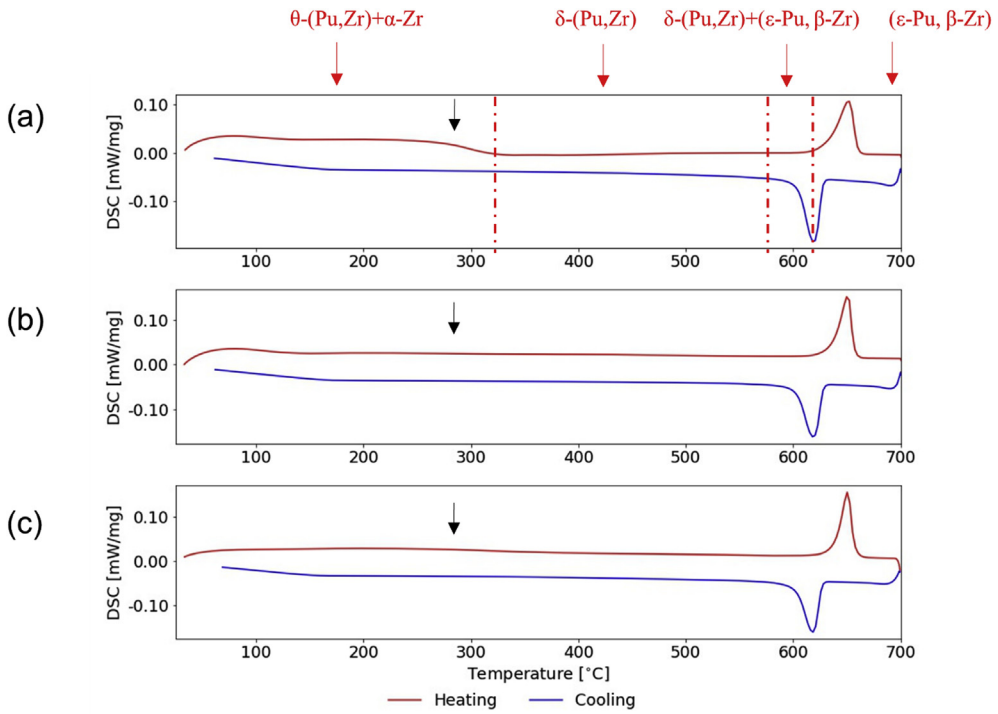

Fig. 6. DSC signal vs. temperature (℃) for Pu – 30Zr upon heating and cooling: (a) First thermal cycle; (b) Second thermal cycle of the as-cast material; (c) Thermal cycle of the annealed material. The phases transition lines estimated from the phase diagrams are outlined by red dashed lines for reader's convenience. The predicted phases for the Pu–Zr binary system are provided in red on top of the graph. (For interpretation of the references to colour in this figure legend, the reader is referred to the Web version of this article.)

Table 1
Calculated peak data from DSC measurements for Pu – 30Zr upon heating.

Fig. 6	Onset T[a] (℃)	Peak T[a] (℃)	End T[a] (℃)	Onset T[a] (℃)	Peak T[a] (℃)	End T[a] (℃)	Description
(a)	268.4	n/a	321.2	631.0	651.4	660.0	As-cast 1st heat
(b)	n/a	n/a	n/a	635.7	650.9	656.8	As-cast 2nd heat
(c)	n/a	n/a	n/a	638.4	650.7	657.1	Annealed

[a] The uncertainty on all temperature values is ±1.5.

Table 2
Calculated peak data from DSC measurements for Pu – 30Zr upon cooling.

Fig. 6	Onset T[a] (℃)	Peak T[a] (℃)	End T[a] (℃)	Description
(a)	627.7	619.2	604.4	As-cast 1st heat
(b)	627.9	618.5	603.2	As-cast 2nd heat
(c)	626.7	618.1	602.5	Annealed

[a] The uncertainty on all temperature values is ±1.5.

sluggish nature and maintaining near-equilibrium state in Pu-based systems is challenging [3,13,16]. Furthermore, the current knowledge dictates that θ-(Pu–Zr) is thermodynamically favored over δ-(Pu,Zr) phase [3,13,16]. Our data indicates that θ-(Pu–Zr) is metastable and can be observed within a small temperature window (100–300 °C). This was confirmed by consecutive heating cycles, which removed θ-(Pu–Zr) from the system, and that we did not observe any traces of θ-(Pu–Zr) during microstructural characterization.

It is possible that the kinetics of transformation from δ-(Pu,Zr) to θ-(Pu–Zr) are not favorable and that the δ-(Pu,Zr) observed in the alloy was only metastable. The initial alloy microstructure was not at equilibrium, as previously discussed. However, annealing of the alloys above 500 °C should have been sufficient to reduce the amount of non-equilibrium phases present in the alloy and bring it closer to equilibrium. It is possible that annealing for more than 17 h, followed by quenching is required to attain low temperature equilibrium, and further studies should be conducted to draw definitive conclusions. However, we did not observe any θ-(Pu–Zr) in any of the examined specimens. Furthermore, neither set of DSC curves obtained for the as-cast alloy after the second thermal cycle and the annealed alloy feature any phase transitions upon heating in low temperature range. This calls for reevaluation of the binary Pu–Zr phase diagram, with particular attention paid to the existence of θ-(Pu–Zr) and its stability. Further work should be conducted on these alloys to stabilize θ-(Pu–Zr). These findings and our previous examination of the Pu–Zr binary system in Pu-rich region [7] indicate that further work is needed to obtain comprehensive understanding of the Pu-based alloys. Future work should include varying annealing conditions (both temperature and time) and cooling rates (slow cooling vs. quenching) to capture all phases that can be present in these alloys. While not within the scope of this work, authors would like to emphasize the need to reevaluate Pu–Zr phase diagrams utilizing new techniques to improve the fundamental understanding of these systems.

4. Conclusions

In this manuscript, we scrutinized the microstructure and phase transition temperatures of the Pu – 30Zr alloys to identify the phases that can be observed in a binary Pu–Zr system. The

Please cite this article as: A. Aitkaliyeva et al., In search of θ-(Pu,Zr) in binary Pu–Zr: Thermal and microstructural analyses of Pu – 30Zr alloy, Journal of Nuclear Materials, https://doi.org/10.1016/j.jnucmat.2019.151875

microstructural characterization revealed that the matrix is consistent with the δ-(Pu,Zr) phase and contains a large number of α-Zr precipitates. Based on microstructural characterization alone, casting and annealing do not induce the expected δ-(Pu,Zr)→θ-(Pu,Zr)+α-Zr phase transformation. This observation contradicts the current belief that θ-(Pu,Zr) is thermodynamically favored over δ-(Pu,Zr). However, DSC data indicates that θ-(Pu−Zr) is metastable, can only be observed within a narrow temperature range, and is not retained during cooling. Our results show that the phase diagrams are accurate in predicting δ-(Pu,Zr) and α-Zr but not when it comes to the stability of the θ-(Pu,Zr) phase. The existence of the θ-(Pu,Zr) phase should be verified in the future using advanced characterization techniques (such as those employed in this manuscript) and low temperature annealing studies aimed to improve the current understanding of the Pu−Zr phase diagram.

Declaration of competing interest

None.

Acknowledgements

This work was supported by the U.S. Department of Energy, Office of Nuclear Energy under DOE Idaho Operations Office Contract DE-AC07-05ID14517, as part of Fuel Cycle Research and Development (FCRD) program of the US DOE and INL Laboratory Directed Research and Development (LDRD) program. Authors would like to acknowledge the staff of Fuel Manufacturing Facility (FMF), Electron Microscopy Laboratory (EML), and Analytical Laboratory at the Materials and Fuels Complex (MFC) at Idaho National Laboratory and Materials Characterization Suite (MaCS) at the Center of Advanced Energy Studies (CAES) for their effort in fabrication, handling, and transfer of the alloys used in this work.

Appendix A. Supplementary data

Supplementary data to this article can be found online at https://doi.org/10.1016/j.jnucmat.2019.151875.

References

[1] H. Okamoto, Plutonium-Zirconium, J. Phase Equilib. 16 (1995) 287−288.
[2] F.H. Ellinger, W. Miner, D. O'Boyle, Constitution of Plutonium Alloys, Los Alamos Scientific Laboratory of the University of California, Los Alamos, NM, 1968.
[3] J. Marples, The plutonium-zirconium phase diagram, J. Less Common. Met. 2 (1960) 331−351.
[4] J. Taylor, The plutonium-zirconium equilibrium diagram from 0 to 10 at% Zr, J. Nucl. Mater. 30 (1969) 346−350.
[5] A. Bochvar, S. Konobeevskii, V. Kutaitsev, T. Men'shikova, N. Chebotarev, Interaction between plutonium and other metals in connection with their arrangement in Mendeleev's periodic table, in: Proceedings of the UN International Conference on Peaceful Uses of Atomic Energy, 1958, pp. 1177−1191.
[6] Plutonium, in: M. Waldron, A. Kay (Eds.), Third Internaional Conference on Plutonium, Chapman and Hall, London, 1965, 1967.
[7] A. Aitkaliyeva, C. Adkins, J. Hirschhorn, C. McKinney, M. Tonks, F. di Lemma, Microstructural characterization of the as-cast and annealed Pu-10Zr alloy, J. Nucl. Mater. 523 (2019) 80−90.
[8] D. Cromer, The crystal structure of ζ-Pu-Zr, ideal formula Pu28Zr, Acta Crystallogr. B35 (1979) 14−19.
[9] Y. Suzuki, A. Maeda, T. Ohmichi, Phase diagram of the Pu-Zr system in the Zr-rich region, J. Alloy. Comp. 182 (1992) L9−L14.
[10] D. Janney, S. Hayes, Experimentally known properties of U-10Zr alloys: a critical review, Nucl. Technol. 203 (2018) 109−128.
[11] Y. Sohn, M. Dayananda, G. Hofman, R. Strain, S. Hayes, J. Nucl. Mater. 279 (2000) 317.
[12] J. Walden, P. Wallace, J. Magana, X-ray spectrometric analysis of plutonium-zirconium alloys, Appl. Spectrosc. 29 (1975) 175−178.
[13] J. Marples, The Plutonium-Zirconium alloy system, in: UKAEA Report, vol. 3110, AERE-R-, 1959.
[14] K. Bradenburg, H. Putz, M. Berndt, Crystal Impact, Pearson's Crystal Data, Bonn, Germany, 1997.
[15] D. Plamer, S. Palmer, SingleCrystal, CrystalMaker software, Oxfordshire, UK, 2018.
[16] J.A.C. Marples, The lattice parameters of some δ and ε-Plutonium alloys, J. Phys. Chem. Solids 25 (1964) 521−534.